J Eng Math (2008) 61:231–247
DOI 10.1007/s10665-007-9181-3

Ultrafast heating and thermomechanical coupling induced by femstosecond lasers

D. Y. Tzou · Emily J. Pfautsch

Received: 30 October 2006 / Accepted: 26 July 2007 / Published online: 3 September 2007

Abstract This work focuses on the ultrafast thermomechanical waves generated by the hot electrons excited by ultrafast, ultra-intense lasers. The dominating effects during the short-time transient, including ultrafast thermalization and relaxation between electrons and phonons, result in thermomechanical coupling that cannot be described by Fourier's law alone. The various thermomechanical properties are grouped to characterize the ultrafast heating and deformation. A finite-difference differential formulation is used as a general tool to tackle the new set of coupled equations that are formulated to describe the severe impingement of a hot-electron blast in the presence of non-equilibrium heating, rapid expansion/contraction of the metal lattices, phonon relaxation, and thermomechanical coupling.

Keywords Hot-electron blast · Relaxation · Thermalization · Thermomechanical coupling · Volumetric expansion rate

1 Introduction

With the laser pulse shortening into femtoseconds (10^{-15} s) and the laser intensity elevating beyond petawatts (10^{15} W), the ultrafast ultra-intense laser (UUL) has unleashed its full potential in producing extremely clean surfaces on virtually any type of material [1–6]. The unique strength of UUL in material processing, as compared to conventional long-pulse lasers, lies in its extremely short contact with the target. While the locally heated material may still undergo severe distortion [7,8], [9, Chapt. 5], [10,11] and phase explosion [12–14], the blasting force due to highly heated electrons may blast away the distorted lattices mechanically and/or sputter melts before the heat-affected zone widely spreads. The opening thus created in the target material is close to that furnished by cold cuts, making UUL much more attractive than conventional lasers with long heating times when desiring specimen with high finish. To date, ultrafast interactions between UUL and local materials can produce electric fields on the order of 10^{11} volts/cm, magnetic fields on the order of 10^9 Gauss, particle accelerations on the order of $10^{25}g$ (with g being gravity of the Earth), local temperature on the order of 10^{10} K, and localized pressure on the order of 10^5 GPa (as compared to the ultimate strength of 1–2 GPa for most metals). These

D. Y. Tzou (✉) · E. J. Pfautsch
Department of Mechanical and Aerospace Engineering, University of Missouri-Columbia, Columbia MO, USA
e-mail: TzouR@missouri.edu

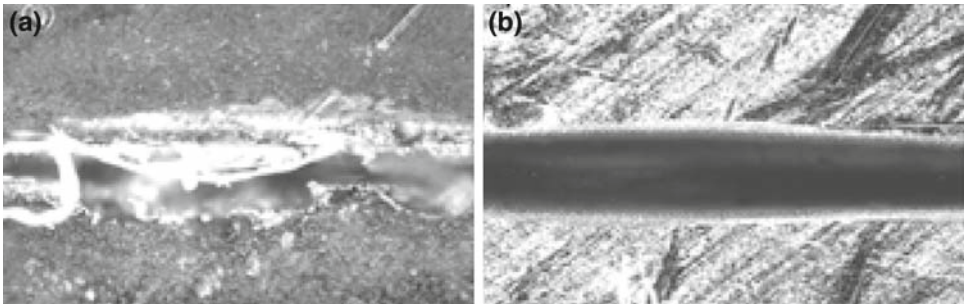

Fig. 1 (**a**) Rough surfaces induced by nanosecond lasers due to long heating time and (**b**) clean surfaces result from ultrashort heating times by femtosecond lasers. Photos Courtesy of Lawrence Livermore Laboratory, the University of California.

extreme conditions only exist in the core of a star or in the vicinity of black holes. Should the refined mechanisms that control the ultrafast irradiation of intense lasers be fully understood, such extreme conditions could become possible on earth. This would lead to a significant expansion of the physical contexts under extreme conditions.

The ways in which heat and load are transmitted through materials play a central role in understanding the refined mechanisms during ultrafast heating and deformation in the femtosecond domain. To inspire further interest in modeling the various competing mechanisms in the ultrafast processes, grooving on stainless steel by a nanosecond laser (a) and by a femtosecond laser (b) is shown in Fig. 1 [1]. Prolonged heating by nanosecond lasers causes melting, resulting in rough surfaces when the liquid phase reconsolidates back into the solid phase, as shown on the left. On the other hand, the same material processed by a femtosecond laser, as shown on the right, results in a strikingly smooth surface in the channel. The smooth surface may result from two different processes. In the first process, there is a spontaneous formation of bubbles in the melt during the femtosecond heating, which drastically increases from about 1 bubble/cm^3 to 10^{26} bubbles/cm^3 due to dynamic nucleation [12–14]. The melt is sputtered away as these bubbles rise altogether. The second process, the hot-electron blast [7–11], results from the nonequilibrium heating of electrons in the femtosecond domain. Fast expansion of the electron gas results in a high pressure that is exerted on the surfaces of the metal lattices, resulting in separations of the lattices as the blasting force becomes excessive. In reality, femtosecond processes may be a combination of both, with the latter being a mechanical process that does not attribute to the phase change of the material.

The mechanical force generated by femtosecond lasers is counterintuitive in nature. Unlike continuous or long-pulse laser heating where damage by the thermal process prevails, femtosecond lasers can produce high-quality surfaces with minimal collateral damage induced by the production of mechanical forces and the intrinsic effects of these forces on the ultrafast deformation of the lattices. With the fundamental understanding developed in previous works [7,8] of the sub-picosecond transient, this work reinstates the effects of volumetric expansion/contraction of the metal lattices, thermal-wave effect for heat propagation in phonons, and thermomechanical coupling through the temperature gradient across the metal lattices. These physical mechanisms follow the hot-electron blast developed in the femtosecond domain, becoming highly activated shortly after the laser pulse. The thermomechanical model incorporates all these effects and is able to describe the ultrafast thermomechanical response covering approximately three orders of magnitude, from tens of femtoseconds (where electron-to-phonon interactions dominate) to tens of picoseconds (where phonon-to-phonon interactions take over). While accommodating the temperature-dependent thermal properties of electrons, the thermophysical parameters that characterize the ultrafast transient will be extracted in terms of nondimensional groups. Their values shall be varied over one to two orders of magnitude in studying their effects on the ultrafast heating and lattice deformation. A finite-difference differential formulation will be developed to tackle the nonlinearly coupled partial differential equations (PDEs), and the formulation will be extended to study the effect of repet-

itive pulsing, as well as the potential effect of plasma shielding due to the surface ionization induced by the UUL.

2 Ultrafast heating

A general formulation for femtosecond heating on metals includes thermal relaxation and thermalization between electrons and phonons (metal lattices) [14,15], energy consumption in support of rapid volumetric expansion/contraction of the metal lattices [9], the blasting force exerted on the metal lattices due to the rapid expansion of the hot electron gas, thermal stresses induced by the temperature gradient in the metal lattices, and temperature-dependent thermomechanical properties of the lattices [7–11]. Due to the significant deviation of the lattice temperature from the reference temperature, particularly beyond 10 picoseconds (threshold value of the relaxation time for phonons) where the metal lattices become highly heated by the hot electrons, the linear theory of thermoelasticity breaks down and nonlinear coupling between the thermal and mechanical fields becomes intrinsic in ultrafast thermomechanics. With all these effects interwoven during the ultrafast transient, the field equations governing the ultrafast response are extremely complicated and nonlinear.

Ultrafast heating is highly nonequilibrium in nature, necessitating separate considerations of energy transport in electrons and phonons with the electron–phonon thermal coupling:

Electrons –

$$C_e\left(T_e\right)\frac{\partial T_e}{\partial t}=\frac{\partial}{\partial x_j}\left[k_e\left(T_e,T_l\right)\frac{\partial T_e}{\partial x_j}\right]-G\left(T_e-T_l\right)+S(x_i,t)\quad\text{with}$$

$$C_e\left(T_e\right)=C_{e0}\left(\frac{T_e}{T_0}\right)\quad\text{and}\quad k_e\left(T_e,T_l\right)=k_{e0}\left(\frac{T_e}{T_l}\right);\tag{1}$$

Phonons –

$$-\frac{\partial q_j^l}{\partial x_j}+G\left(T_e-T_l\right)=C_l\frac{\partial T_l}{\partial t}+\left(\frac{C_l\eta}{\kappa_\varepsilon}\right)\frac{\partial^2 u_j}{\partial t\partial x_j};\quad q_j^l+\tau\frac{\partial q_j^l}{\partial t}=-k_l\frac{\partial T_l}{\partial x_j}\tag{2}$$

where C is the volumetric heat capacity, k the thermal conductivity, G the electron–phonon coupling factor, the subscripts e and l represent electrons and lattices (phonons), respectively, τ the phonon-to-phonon relaxation time, η the thermomechanical coupling factor, κ_ε the thermal expansion coefficient of strain, and the subscript 0 refers to the reference state. The electron–phonon coupling factor, G in W/m^{3}K, is a new property in microscale heat transfer [14–18] that describes the time-rate of exchange of thermal energy between electrons and phonons per unit volume. Thermal relaxation of electrons is neglected in Eq. 1 since the electron-to-electron relation time is only a few femtoseconds. On the other hand, consumption of thermal energy in support of the thermal expansion/contraction of the lattice volume has now been included in Eq. 2 due to the high time-rate of change of the lattice volume $\partial(\partial u_j/\partial x_j)/\partial t$ in the femtosecond domain.[1] The heat capacity of electrons (C_e) increases linearly with the electron temperature as long as $T_e << T_F$, with $T_F = 6.42\times10^4$ K denoting the Fermi temperature. The thermal conductivity of electrons (k_e) in Eq. 1 results from the asymptotic expansion of the general expression [19] in the same limit of $T_e << T_F$:

$$K_e=\chi_1\frac{\left[\left(\frac{T_e}{T_F}\right)^2+0.16\right]^{\frac{5}{4}}\left[\left(\frac{T_e}{T_F}\right)^2+0.44\right]\left(\frac{T_e}{T_F}\right)}{\left[\left(\frac{T_e}{T_F}\right)^2+\chi_2\left(\frac{T_l}{T_F}\right)\right]\sqrt{\left(\frac{T_e}{T_F}\right)^2+0.092}}\cong K_{e0}\left(\frac{T_e}{T_l}\right)\quad\text{for}\quad T_e<<T_F\tag{3}$$

where χ_1 and χ_2 are material constants and $K_{e0}=0.146794\,(\chi_1/\chi_2)$ defines the thermal conductivity at the reference state. The asymptotic expression shown in Eq. 3 is widely used due to its clear indications that (1) $K_e = K_{e0}$

[1] During the fast transient in the femtosecond domain, a volumetric strain ($\partial u_j/\partial x_j$) of the order of nanometers would result in a strain rate ($\partial(\partial u_j/\partial x_j)/\partial t$) on the order of 10^6.

as the electron and phonon are in thermal equilibrium ($T_e = T_l$) at the reference state, and (2) electron conductivity can be many times higher than its equilibrium value as $T_e >> T_l$, which is a typical condition during the initial stage of electron heating by photons since the heat capacity of electrons is about two orders of magnitude lower than that of phonons. Consequently, electron temperature would easily burst into $10^3 - 10^4$ K whereas phonons would still stay thermally undisturbed. Heating of the metal lattices, as seen in Eq. 1, results from heat flow from hot electrons to phonons, which is proportional to the temperature difference ($T_e - T_l$) with the proportional constant being the electron–phonon coupling factor (G). Heating of the metal lattices is thus accomplished in two steps, called the two-step heating model in microscale heat transfer. In consistency with the assumption of $T_e << T_F$ behind Eq. 3, all thermomechanical properties of the metal lattices (phonons) have been treated as constant in the initial stage of ultrafast heating since the renormalization process in support of the property change is of the order of $(T_e/T_F)^2$ [7,8,20]. Under constant phonon properties, the heat-flux vector (q_j^l) in phonons can be eliminated from Eq. 2, resulting in

$$k_l \frac{\partial^2 T_l}{\partial x_j \partial x_j} = C_l \left(\frac{\partial T_l}{\partial t} + \tau \frac{\partial^2 T_l}{\partial t^2} \right) - G \left[(T_e - T_l) + \tau \left(\frac{\partial T_e}{\partial t} - \frac{\partial T_l}{\partial t} \right) \right] + \frac{C_l \eta}{\kappa_\varepsilon} \left[\frac{\partial}{\partial t} \left(\frac{\partial u_j}{\partial x_j} \right) + \tau \frac{\partial^2}{\partial t^2} \left(\frac{\partial u_j}{\partial x_j} \right) \right]. \tag{4}$$

A number of high-order derivatives result due to the high-rate responses, including the lagging behavior describing the delayed response between the heat-flux vector and the temperature gradient in heat transport [9,21–23]. Consequently, special methods developed in classical thermoelasticity assuming Fourier's law heat diffusion, such as Goodier's potential or Boussinesq–Papkovich functions [24, Chapt. 3], no longer hold.

The photon energy carried in the laser beam is absorbed by electrons, with the energy absorption rate S decaying exponentially in space (x_i) and Gaussian in time (t). For the case of a single pulse employing the full-width-at-half-maximum (FWHM) distribution with the initial time shifted from $t = 0$ to $-2t_p$ [14,16], one has

$$S(x_i, t) = 0.94 J \left(\frac{1 - R}{\delta t_p} \right) \exp \left[-\frac{d}{\delta} - 4 \log(2) \left(\frac{t}{t_p} \right)^2 \right] \tag{5}$$

with R being the surface reflectivity, J the laser fluence, δ the radiation penetration depth, $d = \sqrt{x_1^2 + x_2^2 + x_3^2}$ the distance measured from the laser-heated surface, and t_p the pulse duration. The FWHM description aligns the peak of the laser pulse at $t = 0$.

3 Ultrafast deformation—electron blast

Electrons can be viewed as a special type of gas surrounding the metal lattices (phonons) [7,10]. When highly excited, the electron gas rapidly expands, which could result in excessive pressure being exerted on the surfaces of the metal lattices. The equations describing the motion of the metal lattices can be written as

$$\rho \frac{\partial^2 u_i}{\partial t^2} = \frac{\partial \sigma_{ij}}{\partial x_j} + \frac{\partial P_e}{\partial x_i}, \quad \text{with} \quad \sigma_{ij} = \lambda \left(\frac{\partial u_k}{\partial x_k} \right) \delta_{ij} + \mu \left(\frac{\partial u_i}{\partial x_j} + \frac{\partial u_j}{\partial x_i} \right) - \kappa_\sigma \left(T_l - T_0 \right) \delta_{ij} \tag{6}$$

where ρ is the mass density, u_i is the displacement vector of the metal lattice, σ_{ij} is the Cauchy stress tensor, λ and μ are the Lamé constants, κ_σ is the thermal expansion coefficient of stress. Kinetic pressure of the electron gas is represented by P_e,

$$P_e = n k_B T_e \quad \text{with} \quad n = \frac{\pi^2 N}{3} \left(\frac{T_e}{T_F} \right) \quad \Rightarrow \quad P_e = \Lambda T_e^2 \quad \text{with} \quad \Lambda = \frac{\pi^2 N k_B}{3 T_F} \tag{7}$$

with n representing the number density of electrons proportional to the electron temperature (T_e) and number density of atoms (N) and k_B representing the Boltzmann constant. Neglecting the quantum effect, Eq. 7 can be viewed as the equation of state for the electron gas, where the kinetic pressure of electrons is proportional to the electron temperature squared. Substituting Eq. 7 into Eq. 6 results in

$$\rho \frac{\partial^2 u_i}{\partial t^2} = \frac{\partial \sigma_{ij}}{\partial x_j} + 2\Lambda T_e \left(\frac{\partial T_e}{\partial x_i} \right), \tag{8}$$

which displays a driving force due to the rapid expansion of hot electrons. Such a blasting force exerting on the lattice surfaces is proportional to both the temperature and temperature gradient of the electron gas, which will be significant in the early stages of electron heating as described by Eq. 1. Combination of the two equations in Eq. 6 gives

$$\rho \frac{\partial^2 u_i}{\partial t^2} = (\lambda + \mu) \frac{\partial}{\partial x_i} \left(\frac{\partial u_k}{\partial x_k} \right) + \mu \frac{\partial^2 u_i}{\partial x_j \partial x_j} + \Lambda T_e \frac{\partial T_e}{\partial x_i} - \kappa_\sigma \frac{\partial T_l}{\partial x_i} \tag{9}$$

which includes explicit effects from both T_e (through the hot-electron blast) and T_l (thermomechanical coupling) on the motion of the metal lattices.

Equations 1, 4, and 9 were derived from the Boltzmann transport equation [15] and the nonequilibrium partition functions for electrons [20]. Rather than solving them in the microstructural frameworks for electrons and phonons, the continuum formulation as shown absorbs the microstructural effects in additional terms led by the new coefficients. They are the relaxation time (τ) and electron–phonon coupling factor (G) in Eq. 4 and the electron pressure constant (Λ) in Eq. 9. This formulation should hold as long as the physical ground for stress (and consequently the elastic moduli in general) and temperature (hence the thermal conductivity or diffusivity) holds, which, however, will break down as the conductor is composed of only a few lattices.

4 One-dimensional example

Unique features in ultrafast heating and deformation, as shown by Eqs. 1, 4, and 9, lie in the thermomechanical response in time. Consideration of a one-dimensional case, in space, therefore, is sufficient to develop the full resolution during the ultrafast transient. Considering the lattice motion in a one-dimensional film with lateral constraints, the plane-strain condition applies and the one-dimensional forms of Eqs. 1, 4, and 9 are

$$\begin{aligned}
&\left(\frac{C_{e0}}{T_0} \right) T_e \frac{\partial T_e}{\partial t} = k_0 \frac{\partial}{\partial x} \left(\frac{T_e}{T_l} \frac{\partial T_e}{\partial x} \right) - G\,(T_e - T_l) = 0.94J \left(\frac{1-R}{\delta t_p} \right) \exp\left[-\frac{x}{\delta} - 4\log(2) \left(\frac{t}{t_p} \right)^2 \right], \\
&k_l \frac{\partial^2 T_l}{\partial x^2} = C_l \left(\frac{\partial T_l}{\partial t} + \tau \frac{\partial^2 T_l}{\partial t^2} \right) - G \left[(T_e - T_l) + \tau \left(\frac{\partial T_e}{\partial t} - \frac{\partial T_l}{\partial t} \right) \right] + \frac{C_l \eta}{\kappa_\varepsilon} \left(\frac{\partial^2 u}{\partial t \partial x} + \tau \frac{\partial^3 u}{\partial t^2 \partial x} \right), \\
&\rho \frac{\partial^2 u}{\partial t^2} - E_1 \frac{\partial^2 u}{\partial x^2} + E_2 \kappa_\sigma \frac{\partial T_l}{\partial x} = 2\Lambda \left(T_e \frac{\partial T_e}{\partial x} \right), \quad \text{with } E_1 = \frac{E(1-\nu)}{(1+\nu)(1-2\nu)}, \quad E_2 = \frac{E}{1-2\nu}.
\end{aligned} \tag{10}$$

The spatial variable x in (10) describes the distance measured from $x = 0$, the surface subject to the laser irradiation. Heat loss from the film surfaces is negligible during the femtosecond transient,

$$\frac{\partial T_e}{\partial x} = 0, \quad q_l = 0 \quad \text{at} \quad x = 0 \quad \text{and} \quad x = l \tag{11}$$

with l denoting the film thickness. The front and rear surfaces of the film are assumed strain-free,

$$\frac{\partial u}{\partial x} = 0 \quad \text{at} \quad x = 0 \quad \text{and} \quad x = l, \tag{12}$$

whereas the film is assumed to be heated from a stationary state:

$$T_e = T_0, \quad T_l = T_0, \quad \frac{\partial T_l}{\partial t} = 0, \quad \text{and} \quad \frac{\partial u}{\partial t} = 0 \quad \text{as} \quad t = t_0 = -2t_p. \tag{13}$$

The strain-free boundary conditions described in Eq. 12 are employed to tackle the ultrafast response in a simpler situation. For stress-free conditions, Eq. 12 is replaced by

$$\sigma = E_1 \frac{\partial u}{\partial x} - E_2 \kappa_\varepsilon T_l = 0, \quad \text{or} \quad \frac{\partial u}{\partial x} = \left(\frac{E_2}{E_1}\right) \kappa_\varepsilon T_l \quad \text{at} \quad x = 0 \quad \text{and} \quad x = l \tag{14}$$

which relate the surface strains to the surface temperatures of phonons.

To characterize the ultrafast response in terms of the dominating parameters, Eqs. 10–13 are made dimensionless by introducing

$$\xi = \frac{x}{\delta}, \quad \beta = \frac{t}{t_p}, \quad \theta_{e(l)} = \frac{T_{e(l)}}{T_0}, \quad U = \frac{u}{\left(\Lambda T_0^2 t_p^2/\rho\delta\right)}, \quad Y = \frac{E_0/\rho}{(\delta/t_p)^2}, \quad \beta_0 = \frac{t_0}{t_p},$$

$$S = 0.94J\left(\frac{1-R}{\delta C_{e0} T_0}\right), \quad H = \frac{G t_p}{C_{e0}}, \quad K = \frac{\alpha_0 t_p}{\delta^2}, \quad C = \frac{C_{e0}}{C_l}, \quad L = \frac{l}{\delta}, \quad \alpha_0 = \frac{k_{e0}}{C_{e0}},$$

$$M = \frac{\eta}{\left(\frac{\rho\delta^2\kappa_\varepsilon}{\Lambda T_0 t_p^2}\right)}, \quad \Gamma = \frac{\tau}{t_p}, \quad Y_1 = \frac{E_1 t_p^2}{\rho\delta^2}, \quad Y_2 = \frac{E_2\kappa_\varepsilon}{\Lambda T_0}, \tag{15}$$

Equations 10–13 become

$$\theta_e \frac{\partial\theta_e}{\partial\beta} = K\frac{\partial}{\partial\xi}\left(\frac{\theta_e}{\theta_l}\frac{\partial\theta_e}{\partial\xi}\right) - H(\theta_e - \theta_l) + S\exp\left[-\xi - 4\log(2)\beta^2\right],$$

$$KC\frac{\partial^2\theta_l}{\partial\xi^2} = \Gamma\frac{\partial^2\theta_l}{\partial\beta^2} + \frac{\partial\theta_l}{\partial\beta} - HC\left[(\theta_e - \theta_l) + \Gamma\frac{\partial}{\partial\beta}(\theta_e - \theta_l)\right] + M\left(\frac{\partial^2 U}{\partial\beta\partial\xi} + \Gamma\frac{\partial^3 U}{\partial\beta^2\partial\xi}\right),$$

$$\frac{\partial^2 U}{\partial\beta^2} - Y_1\frac{\partial^2 U}{\partial\xi^2} + Y_2\frac{\partial\theta_l}{\partial\xi} = 2\theta_e\frac{\partial\theta_e}{\partial\xi}. \tag{16}$$

Ultrafast heating and deformation is thus characterized by seven parameters: K (nondimensional thermal diffusivity of electrons), H (nondimensional electron–phonon coupling factor), S (nondimensional laser fluence), C (heat-capacity ratio), Γ (nondimensional relaxation time of phonons), M(nondimensional group of thermomechanical coupling), Y_1 (nondimensional elastic modulus), and Y_2 (nondimensional thermoelastic modulus). Equation 16 provides three equations to be solved for three unknowns, θ_e, θ_l, and U, subjected to the initial and boundary conditions:

$$\theta_e = \theta_l = 1, \quad \frac{\partial\theta_l}{\partial\beta} = 0, \quad \text{and} \quad \frac{\partial U}{\partial\beta} = 0 \quad \text{as} \quad \beta = -2; \tag{17}$$

$$\frac{\partial\theta_e}{\partial\xi} = 0, \quad \frac{\partial\theta_l}{\partial\xi} = 0, \quad \frac{\partial U}{\partial\xi} = 0 \quad \text{at} \quad \xi = 0 \quad \text{and} \quad x = L. \tag{18}$$

4.1 Surface ionization

In-depth processing of materials by UUL, as shown by the metal grooving in Fig. 1, involves repetitive applications of a series of laser pulses. For UUL beyond terawatts, surface ionization (plasma formation) is possible after the first few pulses, which forms a layer of ion clouds that shields the metal surface from the subsequent laser pulses. The energy absorption rate by electrons, as described by the last term in the first expression of Eq. 10 or 16, therefore, needs to be modified to account for the energy dissipation through the plasma. A phenomenological approach is to

accommodate the length-absorption coefficient (α_p, in m^{-1}) and the plasma formation time (t_i, in seconds) in the energy absorption rate in electrons [25]:

$$\begin{cases} 0.94J\left(\dfrac{1-R}{\delta t_p}\right)\exp\left[-\dfrac{x}{\delta}-4\log(2)\left(\dfrac{t}{t_p}\right)^2\right] & \text{for} \quad t < t_i \\ 0.94J\left(\dfrac{1-R}{\delta t_p}\right)\exp\left[-\dfrac{x}{\delta}-4\log(2)\left(\dfrac{t}{t_p}\right)^2\right]\times\exp\left[-\alpha_p c\,(t-t_i)\right] & \text{for} \quad t \geq t_i \end{cases} = S f_s(\xi,\beta);$$

$$f_s(\xi,\beta) = \begin{cases} \exp\left[-\xi-4\log(2)\beta^2\right] & \text{for} \quad \beta < \beta_i \\ \exp\left[-\xi-4\log(2)\beta^2\right]\times\exp\left[-A\,(\beta-\beta_i)\right] & \text{for} \quad \beta \geq \beta_i \end{cases} \tag{19}$$

where $A = \alpha_p c t_p$ and $\beta_i = t_i/t_p$, with c denoting the speed of light. The effect of energy dissipation in plasma is described by the normalized intensity function f_s, which is characterized by two additional parameters: the nondimensional plasma absorption coefficient (A) and the nondimensional plasma-formation time (β_i). Both values are material-dependent. With the energy intensity remaining the same before the plasma formation ($\beta < \beta_i$), as shown in Figs. 8 and 9, the energy absorbed by electrons can be significantly reduced after the plasma formation ($\beta \geq \beta_i$). Reduction of the energy intensity is more significant under a larger value of A (stronger dissipation in plasma) or a smaller value of β_i (earlier shielding by plasma). For the subsequent laser pulse blocked by the plasma layer, Eq. 19 replaces the last term of the first expression in Eq. 16.

A quantitative analysis for the plasma formation involves more than a simple modification of the energy-absorption rate. It involves a fluidized heat-transfer model for the ionic flows, along with the physical onset for ionization, as well as the additional conservation law for charges. Further complications also include the ablated materials mixing with the ions, which makes the fluidized ionic flow two-phase by nature. Such a general approach adds an additional set of conservation equations to Eq. 16, which will appear in another work in progress.

4.2 Finite-difference differential formulation

Even without incorporating the temperature-dependence of lattice properties, Eq. 16 displays a set of three nonlinearly coupled PDEs. Continuing the previous efforts in developing efficient numerical algorithms to resolve the various tangling effects [7–11], the nonlinearly coupled PDE will be solved in this work by the combined finite-difference differential method [26, Chapt. 20]. The idea is simple and intuitive. We apply the central-difference formula to approximate all the space (ξ) derivatives in Eq. 16, which results in a set of nonlinear coupled ordinary differential equations (ODE) in the time (β) domain. The resulting ODEs in β are then solved by standard ODE solvers, such as NDSolve in *Mathematica* [27]. Decomposing the film thickness (L) into N nodes, with i being the nodal number,

$$\frac{\partial^2 X_i}{\partial\xi} \to \frac{X_{i+1}+X_{i-1}-2X_i}{(\Delta\xi)^2}, \quad \frac{\partial X_i}{\partial\xi} \to \frac{X_{i+1}-X_{i-1}}{2\,(\Delta\xi)}, \quad \Delta\xi = \frac{L}{N-1} \tag{20}$$

the equations of (16) become

$$\theta_e^i\frac{\mathrm{d}\theta_e^i}{\mathrm{d}\beta} = K\left\{\left(\frac{\theta_e^i}{\theta_l^i}\right)\left[\frac{\theta_e^{i+1}+\theta_e^{i-1}-2\theta_e^i}{(\Delta\xi)^2}\right]+\frac{1}{\theta_l^i}\left[\frac{\theta_e^{i+1}-\theta_e^{i-1}}{2\,(\Delta\xi)}\right]^2-\left[\frac{\theta_e^i}{(\theta_l^i)^2}\right]\left[\frac{\left(\theta_e^{i+1}-\theta_e^{i-1}\right)\left(\theta_l^{i+1}-\theta_l^{i-1}\right)}{4\,(\Delta\xi)^2}\right]\right.$$
$$\left.-H\left(\theta_e^i-\theta_l^i\right)+S\exp\left[-(i-1)\Delta\xi-4\log(2)\beta^2\right]\right\},$$

$$\Gamma\frac{\mathrm{d}^2\theta_l^i}{\mathrm{d}\beta^2}+\frac{\mathrm{d}\theta_l^i}{\mathrm{d}\beta}=KC\left[\frac{\theta_l^{i+1}+\theta_l^{i-1}-2\theta_l^i}{(\Delta\xi)^2}\right]+HC\left[\left(\theta_e^i-\theta_l^i\right)+\Gamma\frac{\mathrm{d}}{\mathrm{d}\beta}\left(\theta_e^i-\theta_l^i\right)\right]$$
$$-M\frac{\mathrm{d}}{\mathrm{d}\beta}\left[\frac{U_{i+1}-U_{i-1}}{2\,(\Delta\xi)}\right]-M\Gamma\frac{\mathrm{d}^2}{\mathrm{d}\beta^2}\left[\frac{U_{i+1}-U_{i-1}}{2\,(\Delta\xi)}\right],$$
$$\frac{\mathrm{d}^2U_i}{\mathrm{d}\beta^2}=2\theta_e^i\left[\frac{\theta_e^{i+1}-\theta_e^{i-1}}{2\,(\Delta\xi)}\right]+Y_1\left[\frac{U_{i+1}+U_{i-1}-2U_i}{(\Delta\xi)^2}\right]-Y_2\left[\frac{\theta_l^{i+1}-\theta_l^{i-1}}{2\,(\Delta\xi)}\right],\quad i=2,3,\ldots,(N-1). \tag{21}$$

The zero slopes in Eq. 18 are assured by applying the forward-difference formula:

$$\theta_e^1(\beta)=\theta_e^2(\beta),\quad \theta_l^1(\beta)=\theta_l^2(\beta),\quad U_1(\beta)=U_2(\beta),\theta_e^N(\beta)=\theta_e^{N-1}(\beta)$$
$$\theta_l^N(\beta)=\theta_l^{N-1}(\beta),\quad U_N(\beta)=U_{N-1}(\beta). \tag{22}$$

Equations 21 and 22 provide $3N$ ordinary differential equations, in β (time), to be solved for $\theta_e^i(\beta)$, $\theta_l^i(\beta)$, and $U_i(\beta)$, each of which satisfying the initial conditions in (17):

$$\theta_e^i=\theta_l^i=1,\quad \frac{\mathrm{d}\theta_l^i}{\mathrm{d}\beta}=0,\quad \text{and}\quad \frac{\mathrm{d}U_i}{\mathrm{d}\beta}=0\quad \text{as}\quad \beta=-2,\quad i=1,2,\ldots,N. \tag{23}$$

The coupled set of ODEs in β are solved by a direct use of NDSolve in *Mathematica*, which adapts the step size so that the estimated error in the solution is within the tolerances specified by PrecisionGoal (for suppressing the relative local error allowed at each step) and AccuracyGoal (for suppressing the absolute local error allowed at each step). The value of N is continuously doubled until convergence of the solutions is achieved. The results presented in this work result from the use of $N=40$. The finite-difference differential formulation shown in (21) is similar to the method of lines encoded in NDSolve for solving partial differential equations. The formulation is particularly suitable for studying the ultrafast response with complicated structures in time, including those resulting from the combined behavior of thermalization and relaxation in microscale heat transfer [26]. Due to effective reductions of PDEs, either linear or nonlinear, to ODEs whose solution algorithms are much better developed, the finite-difference differential method has been extended, and well tested, for various problems in classical elasticity (direct solutions to Navier's equations), fluid mechanics (Navier–Stokes equations with nonlinear coupling and/or injection/suction at the boundaries), and heat-transfer (direct calculation of the heat-transfer coefficient in the presence of boundary slippage). Direct use of NDSolve in *Mathematica* using this approach has been shown to be capable of tackling solutions that were not possible before. It can be used in place of the experience-dependent approaches such as the semi-inverse method in elasticity/thermoelasticity or the similarity solutions in fluid mechanics/heat transfer, which are often difficult to beginners.

5 Numerical results

Numerical solutions to Eqs. 21–23 are obtained for a gold film with the following thermal and optical properties: $k_{e0}=315\,\mathrm{W/mK}$, $C_{e0}=2.1\times10^4\,\mathrm{J/m^3\,K}$, $\tau=10\,\mathrm{ps}$, $C_l=2.5\times10^6\,\mathrm{J/m^3\,K}$, $g=2.6\times10^{16}\,\mathrm{J/m^3\,K}$, $\delta=15.3\,\mathrm{nm}$, $R=0.93$, $T_0=300\,\mathrm{K}$, and $l=0.02\,\mu\mathrm{m}$ [7–9]. Mechanical properties for gold are $E=79\,\mathrm{GPa}$, $\nu=0.42$, $\kappa_\varepsilon=14.2\times10^{-6}$, and $\Lambda=10^5\,\mathrm{J/m^3\,K}$. The laser fluence is taken to be $J=732\,\mathrm{J/m^2}$. The non-dimensional parameters are thus $H\cong0.124$, $K\cong6.41$, $C\cong8.4\times10^{-3}$, $\Gamma\cong100$, $M=6.4915\times10^{-5}$, $Y_1=4.46376\times10^{-4}$, $Y_2=0.27156$, $S_0=500$, and $L=1.307$. These values will be used throughout the numerical analyses, unless stated otherwise.

Electron and phonon temperatures are not sensitive to K, C, and Γ [7,8] during ultrafast heating. Varying each of these parameters individually by 2 to 3 orders of magnitude only affects the temperature response by less than 20% with all the qualitative trends remaining the same. The effect of H is shown in Fig. 2(a), where electron and phonon temperatures are grouped with the same value of H, represented by similar line styles. For conversions to

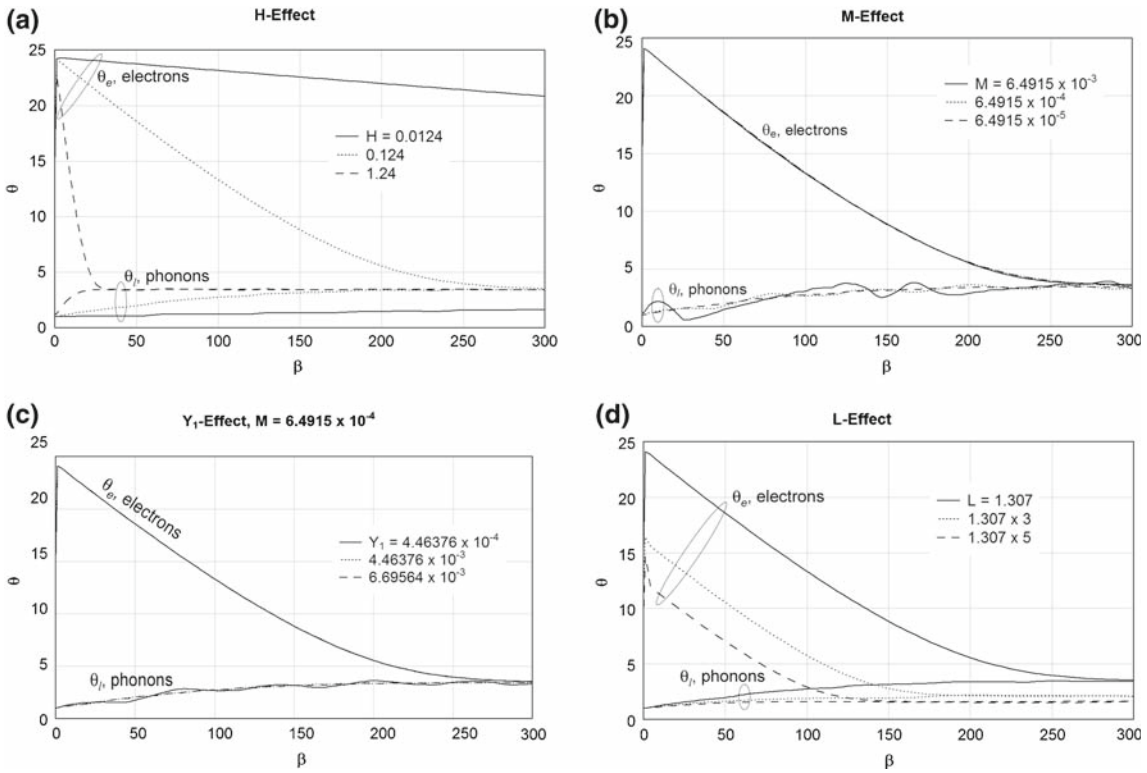

Fig. 2 Non-equilibrium heating of electrons and phonons: (**a**) Effect of H, (**b**) effect of M, and (**c**) effect of Y_1, and (**d**) effect of L. Other parameters are not sensitive

real scales, $\beta = 1$ is equivalent to $t = 0.1$ ps and $\theta_{e,l} = 1$ is equivalent to $T_{e,l} = 300$ K. The electron temperature decreases very rapidly as the value of $H(\sim G)$ increases, since a larger value of H implies a higher rate of energy flow from electrons to phonons. The peak temperature of electrons also decreases as the value of H increases. On the contrary, as phonons receive the energy from electrons at a higher rate, their temperatures increase with the value of H. The thermalization time between electrons and phonons, i.e., the time at which $\theta_e = \theta_l$, decreases as the value of H increases. For $H = 1.24$, as shown by the dashed line in Fig. 2(a), thermal equilibrium between electrons and phonons is achieved as $\beta \cong 25$ ($t = 2.5$ ps).

Parameter M measures the effect of energy consumed in support of the ultrafast expansion of the lattice volumes in ultrafast heating, which has often been neglected in classical thermoelasticity. It is an explicit parameter appearing in Eq. 16, the energy equation for phonons, which has been recovered to account for the large volumetric strain rate of phonons during the femtosecond transient. The electron temperature is almost unaffected as the value of M increases by two orders of magnitude, which is shown in Fig. 2(b). The phonon temperature, however, starts to oscillate as M increases to 6.4915×10^{-3} due to the high-frequency expansion/contraction of the metal lattices in high-rate heating. The overall sensitivity of electron/phonon temperatures to M is far less than that to H.

Parameter Y_1 does not appear explicitly in the energy equation for phonons, Eq. 16, but it could affect the phonon temperature through the volumetric strain rate, $M\frac{\partial^2 U}{\partial\beta\partial\xi}$, in Eq. 16. In the medium case of $M = 6.4915 \times 10^{-4}$, Fig. 2(c), oscillations in the phonon temperature (due to the expansion/contraction of the metal lattices shown in Fig. 2(b)) are effectively suppressed as the value of Y_1 increases from 4.46376×10^{-4} to 6.69564×10^{-3}. The parameter Y_1 can also be viewed as the nondimensional dilatational wave speed squared. A larger value of Y_1 implies a faster speed of dilatational waves, which would bounce more frequently between the front and rear surfaces of the film under the same thickness. Consequently, the ripples in the phonon temperature are flattened by the reflected waves in the case of a larger value of Y_1. The change in the magnitude of phonon temperatures through the indirect strain-rate

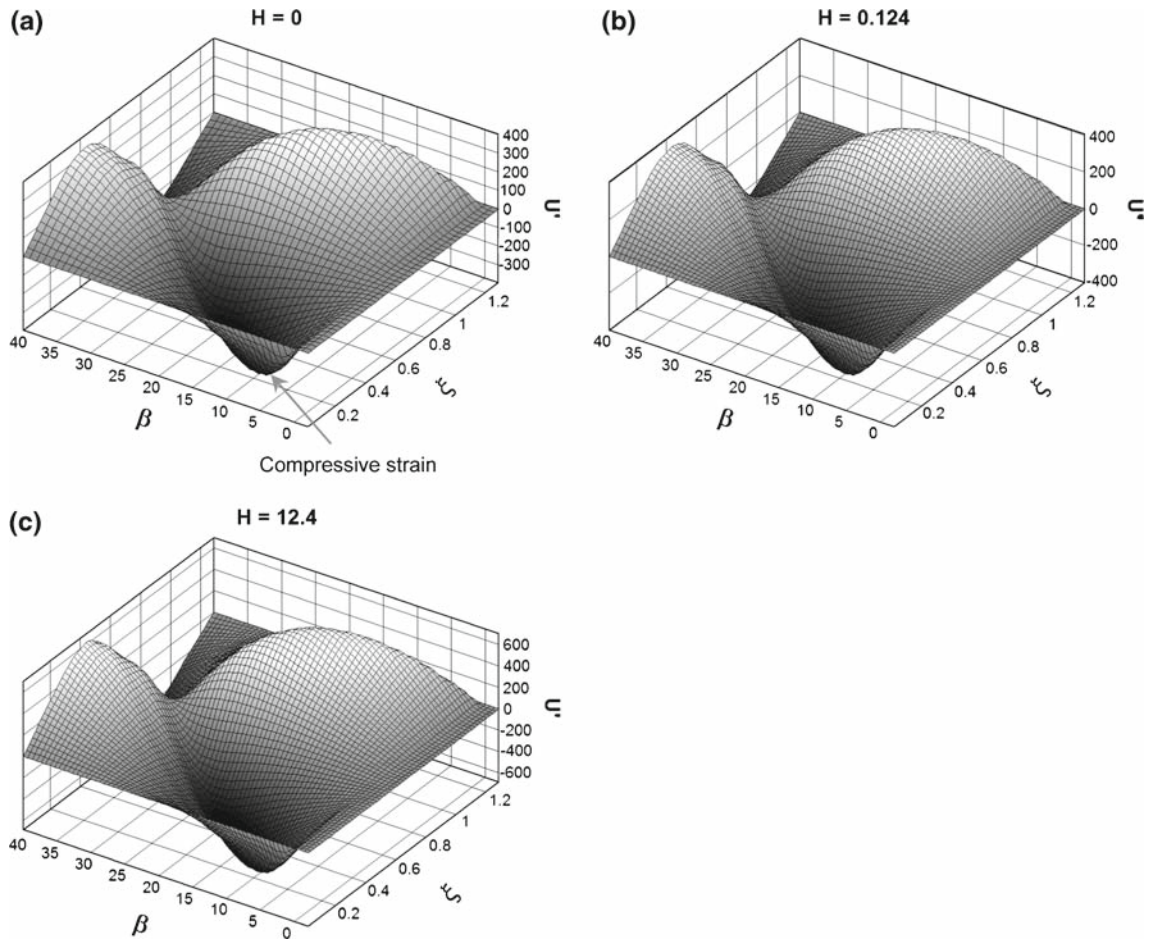

Fig. 3 Straining patterns, $U'(\xi, \beta)$, developed in the gold film—Effect of H

coupling, however, is less than 10% at all times. Through the same coupling factor M, neither the electron nor the phonon temperature varies appreciably as the value of Y_2 increases/decreases by two orders of magnitude from the threshold.

Figure 2(d) displays the effect of film thickness on the electron and phonon temperatures. A thicker film, as expected, results in a lower temperature for both electrons and phonons due to the larger physical domain in dissipating heat by conduction. Note that thermalization between electrons and phonons is significantly faster in thinner films, at $\beta \cong 150$ (15 ps) in the case of $L = 6.52$(0.1 μm) as compared to $\beta \cong 300$ in the case of $L = 1.307$.

Parameter H is an explicit parameter characterizing the electron (θ_e) and phonon (θ_l) temperatures in (16), having drastic effects on the electron and phonon temperatures as shown in Fig. 2(a). With regard to the ultrafast deformation in the gold film, on the other hand, the parameter H becomes an implicit parameter, which enters the equation of motion through the gradients of θ_e and θ_l. Figure 3 describes the straining patterns developed in the gold film as the parameter H varies from 0 (no energy exchange between electrons and phonons) to 12.4. The hot-electron blast, $2\theta_e \partial\theta_e/\partial\xi$ in Eq. 16, introduces compressive strains ($U' < 0$) on the initial contact ($\beta = 0$) with the film (near $\xi = 0$), as indicated in Fig. 3(a). The peak of the compressive strain is located between the characteristic lines of thermal and mechanical waves [7,8]. After the initial compressive strain near the front surface, two tensile ripples follow, in the direction of increasing time (β increases) or in the direction toward the interior of the film (ξ increases). Another compressive ripple results near the back surface of the film ($\xi > 0.8$) at longer times ($\beta > 20$). Such alterations between compressive and tensile strains prevail in the temporal and spatial directions,

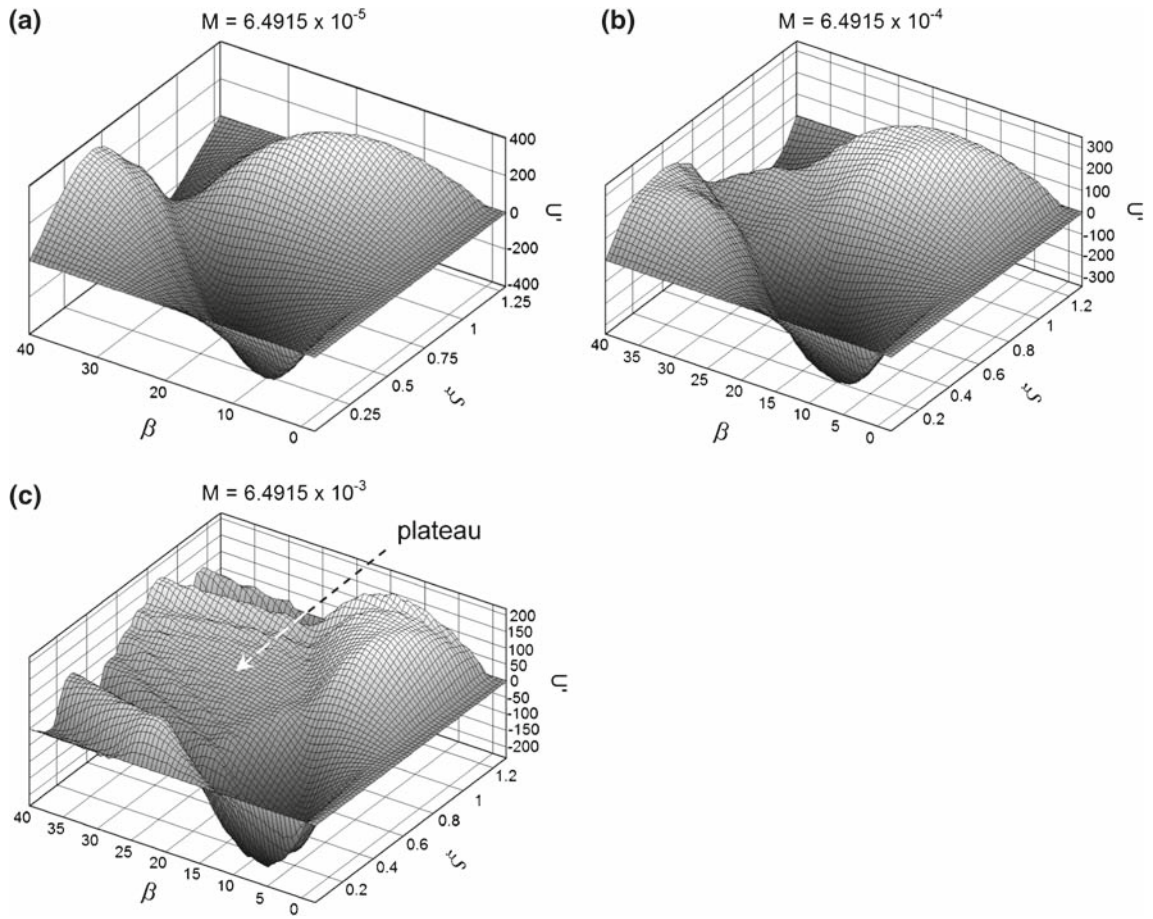

Fig. 4 Straining patterns, $U'(\xi, \beta)$, developed in the gold film—Effect of M

which become even more exaggerated at longer times due to reflections of the displacement waves from the front ($\xi = 0$) and rear ($\xi = 1.307$) surfaces of the film. As the value of H increases, the peak values of compressive and tensile strains slightly increase. All qualitative features of the straining patterns, however, remain the same.

The volumetric expansion/contraction rate characterized by the parameter M in Eq. 16 has pronounced effects on the straining patterns, as shown in Fig. 4. As the value of M increases from 6.4915×10^{-5} to 6.4915×10^{-3}, with the initial compressive strain prevailing near the front surface of the film, the volumetric expansion/contraction rate effectively suppresses the tensile strains and produces a plateau in the interior of the film for $\beta > 20$. The plateau results from the sign change of $(\partial\theta_l/\partial\xi)$, as shown in Fig. 2(b). The compressive (tensile) strains in place are cancelled by the tensile (compressive) strains as the time-rate of change of the temperature gradient switches its sign.

The value of M is increased from the threshold 6.4915×10^{-5} to 6.4915×10^{-4} in Fig. 5 to better describe the effect of thermal waves. In the presence of thermal relaxation in phonons, referring to the second expression in Eq. 16, the nondimensional thermal-wave speed is $\sqrt{KC/\Gamma}$, with Γ being the nondimensional relaxation time of phonons. When assuming an infinite speed of heat propagation, Fouriers law is recovered as $\Gamma \to 0$, which corresponds to the case with a smaller value of Γ in Fig. 5(a). In the presence of a stronger effect from the volumetric expansion/contraction rate, $M = 6.4915 \times 10^{-4}$ as compared to the threshold of 6.4915×10^{-5} for gold, compressive strain induced by the thermomechanical coupling from Fourier diffusion is suppressed in the interior of the film at longer times, $0.8 < \xi < 1$ and $\beta > 25$ in Fig. 5(a). As the effect of thermal relaxation in phonons

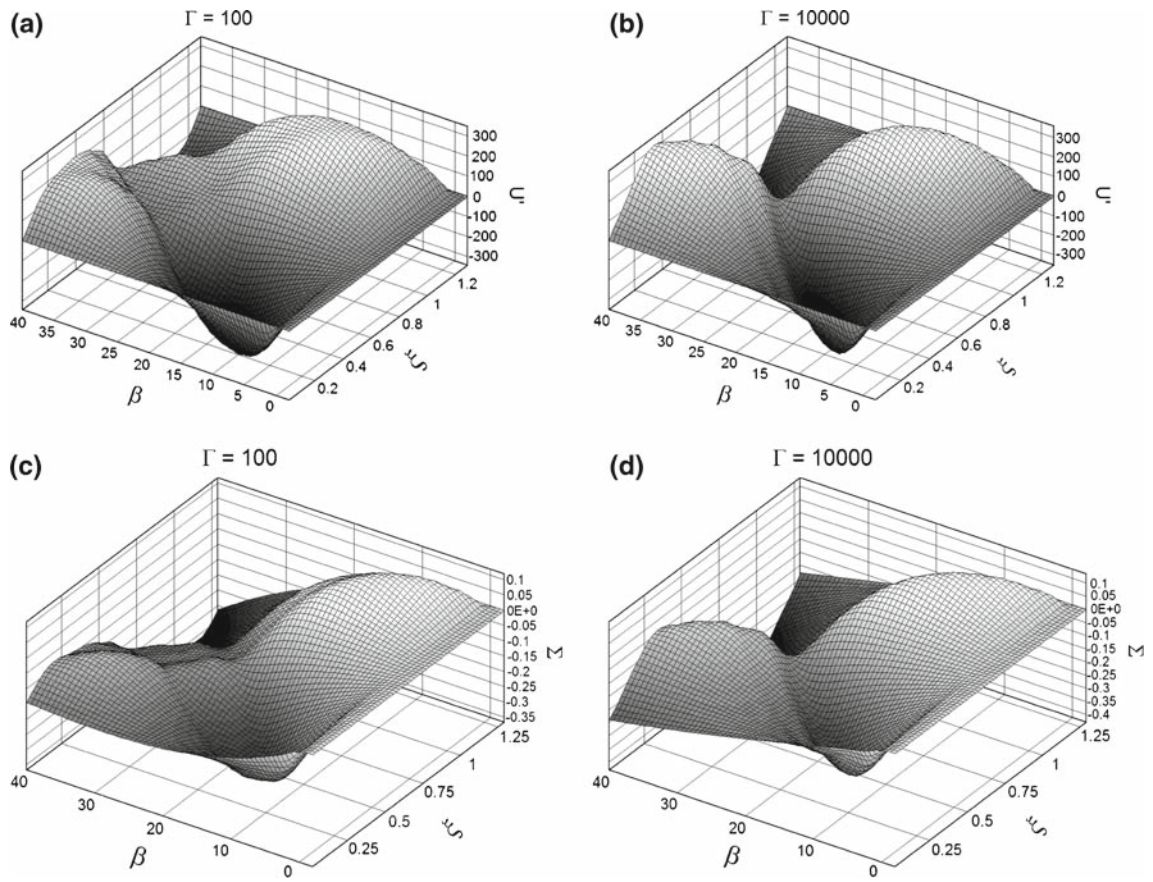

Fig. 5 Strain ($U'(\xi, \beta)$) and stress ($\Sigma(\xi, \beta)$) patterns developed in the gold film—Effect of Γ for $M = 6.4915 \times 10^{-4}$

becomes strong, $\Gamma = 10^4$ in Fig. 5(b) with the characteristic line of thermal waves located at $\xi \pm 2.32 \times 10^{-3}\beta$, strong compression in front of the thermal wave recovers the compressive strain, showing a deep valley behind the two tensile ripples ($U' > 0$) in Fig. 5(b). Thermal stresses can be calculated from the generalized Hooke's law,

$$\sigma = E_1 \frac{\partial u}{\partial x} - E_2 \kappa_\varepsilon \left(T_l - T_0\right), \quad \text{or} \quad \Sigma = Y_1 \left(\frac{\partial U}{\partial \xi}\right) - Y_2 \left(\theta_l - 1\right) \quad \text{with } \Sigma = \frac{\sigma}{\Lambda T_0^2}. \tag{24}$$

For $\Gamma = 100$, the case approaching Fourier diffusion in correspondence with Fig. 5(a), Fig. 5(c) displays the thermal-stress pattern developed in the thin film. With severe compression ($\Sigma < 0$ of several GPa) induced by the hot-electron blast in the same location, the surface warping in the interior of the film at longer times, $0.8 < \xi < 1$ and $\beta > 25$ in Fig. 5(a), now becomes even more obvious due to the direct involvement of the lattice temperature in Eq. 24. For $\Gamma = 10000$, likewise, strong compression ahead of the thermal wavefront straightens the wiggling surface, resulting in two distinct valleys in compression. One valley nears the front surface at short times, which is induced by the hot-electron blast, and another valley nears the rear surface at long times, which is contributed by the reflected waves from the rear surface of the film. In comparison with the compressive strains shown in Figs. 5(a) and 5(b), tensile stresses ($\Sigma > 0$) only exist near the peak at short times in Figs. 5(c) and 5(d). The magnitude of tension, however, is about one order of magnitude lower than that of compression. Tensile stresses in the physical domain with compressive strains result from the oscillation of the lattice-temperature shown in Fig. 2(b). The thermal stress is positive ($\Sigma > 0$) in the physical domain where $\theta_l < 1 + \left(\frac{Y_1}{Y_2}\right)\left(\frac{\partial U}{\partial \xi}\right)$ with $\left(\frac{\partial U}{\partial \xi}\right) < 0$.

A faster wave (larger values of Y_1) under the same film thickness, or a thinner film (smaller values of L) under the same wave speed, implies more frequent reflections of dilatational waves between the front and rear surfaces

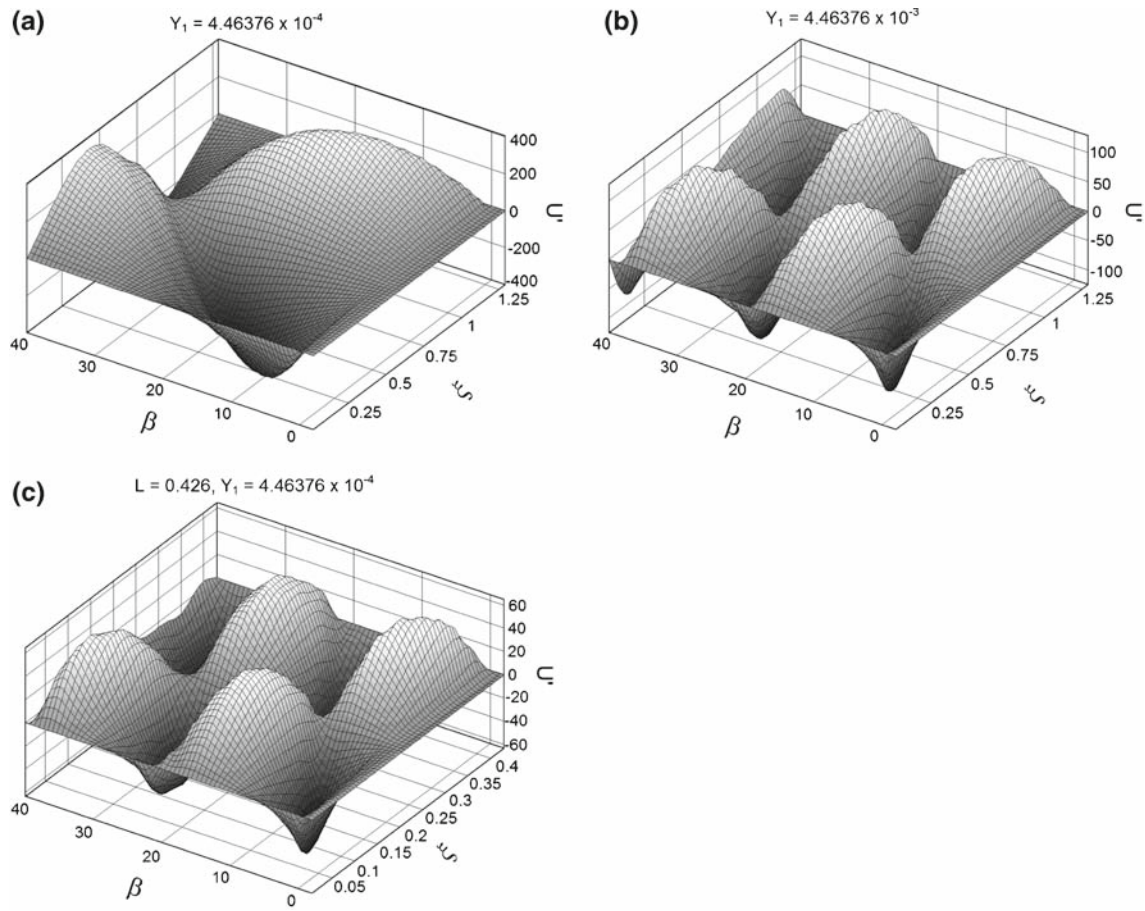

Fig. 6 Effect of Y_1 on straining of the gold film, (**a**) and (**b**), and a similar effect in reduction of the film thickness, (**b**) and (**c**)

of the film. Therefore, more frequent sign changes in strain are expected under these conditions. Figure 6 illustrates this behavior by increasing the value of Y_1 from 4.46376×10^{-4}, Fig. 6(a), to 4.46376×10^{-3}, Fig. 6(b), under the same value of L (1.307). As the value of Y_1 increases by one order of magnitude, the number of strain ripples doubles. A similar behavior can be observed in Figs. 6(a) and 6(c), where the film thickness is reduced by a factor of three under the same value of $Y_1(4.46376 \times 10^{-4})$. More frequent sweeping of dilatational waves across the film results in four pairs of compression-tension waves in the physical domain of $0 < \xi < 1.307$ and $0 < \beta < 40$.

Parameter Y_2, the nondimensional thermoelastic modulus, is one of the two explicit parameters in the equation of motion. It does not have a remarkable effect on the electron or phonon temperatures, but it will have a more pronounced effect in the ultrafast deformation of the thin film. Figure 7 shows the effect of Y_2 on the straining patterns as its value is increased by two orders of magnitude, from $Y_2 = 0.27156$ (Fig. 7(a)) to 27.156 (Fig. 7(c)). With the initial compressive strain (peaked as $\beta \cong 11$) near the front surface and the initial tensile strain near the rear surface (at $\xi \cong 1.16$) remaining, the effect of the thermoelastic modulus is mainly in the interior of the film and at longer times. For $Y_2 = 27.156$, Fig. 7(c), the larger temperature gradient of phonons developed in the interior of the film, i.e., larger values of $\partial\theta_l/\partial\xi$ in Eq. 16, shrinks the compressive region near the rear surface of the film at longer times, making the strain pattern much flatter in $0.5 < \xi < 1.2$ and $25 < \beta < 40$. A large tensile region ($U' > 0$), in fact, exists in this area in place of the compressive region in Figs. 7(a) and 7(b).

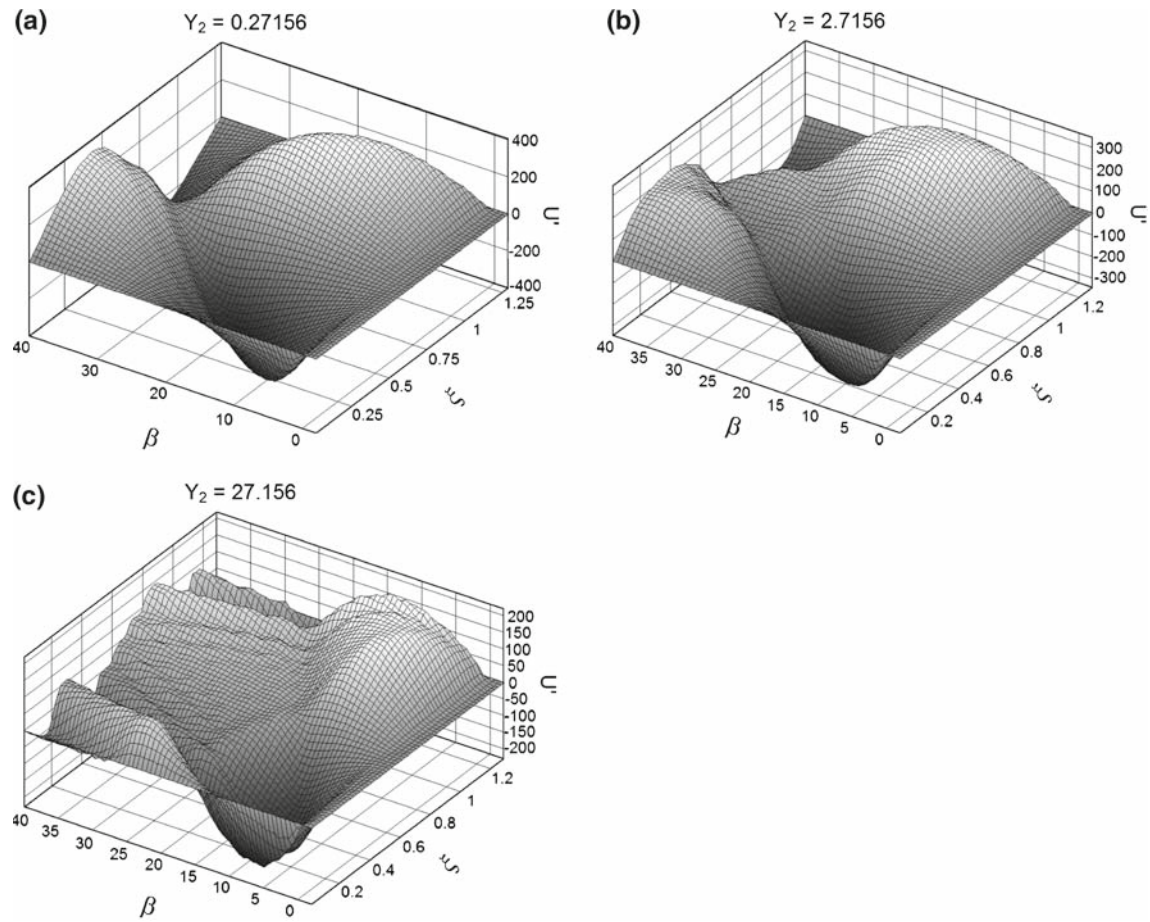

Fig. 7 Effect of Y_2 on straining of the gold film: (**a**) $Y_2 = 0.27156$, (**b**) $Y_2 = 2.7156$, and (**c**) $Y_2 = 27.156$

The effect of ion formation in repetitive pulsing, from the use of Eq. 19 instead of the last term in the first expression of Eq. 16, is shown in Figs. 8 and 9. All threshold values used in Fig. 3(b) are recovered. For the case that surface ionization occurs after $\beta_i \geq 0.2$, Fig. 8 shows the effect of A on the straining patterns developed in the thin film. As the value of A increases from 0 (no ionization) to 50, there is stronger absorption of photons by plasma before the laser pulse reaches the front surface, and the peak values of strain developed at later times decrease by about 35%. This is due to the strong absorption of photons by ions for $\beta_i \geq 0.2$, and consequently the drastic reduction of the energy density, as shown in Fig. 8, is in correspondence. The identical pulse shape (energy density) for $-2 < \beta_i < 0.2$ (before the ionization) is responsible for the preservation of all qualitative features, particularly the strong compression induced by the hot-electron blast near the front surface at short times, which changes little as the value of A increases from 0 to 50.

Under a constant length-absorption coefficient in plasma, $A = 5$, Fig. 9 displays the effect of the plasma-formation time. Again, the normalized energy-density function is attached correspondingly as the value of β_i increases from 0.1, 0.5, to 1. Earlier formation of plasma, $\beta_i = 0.1$ in Fig. 9(a), implies a longer shielding time from the laser pulse. Consequently, it weakens the strain level developed in the thin film. The energy density is gradually recovered as the plasma-formation time lengthens, which corresponds to materials with higher ionization energy. Plasma formation in the case of $\beta_i = 1$, Fig. 9(c), is so late that the full pulse shape is almost recovered, resulting in the same response as that shown in Fig. 3(b) without plasma shielding.

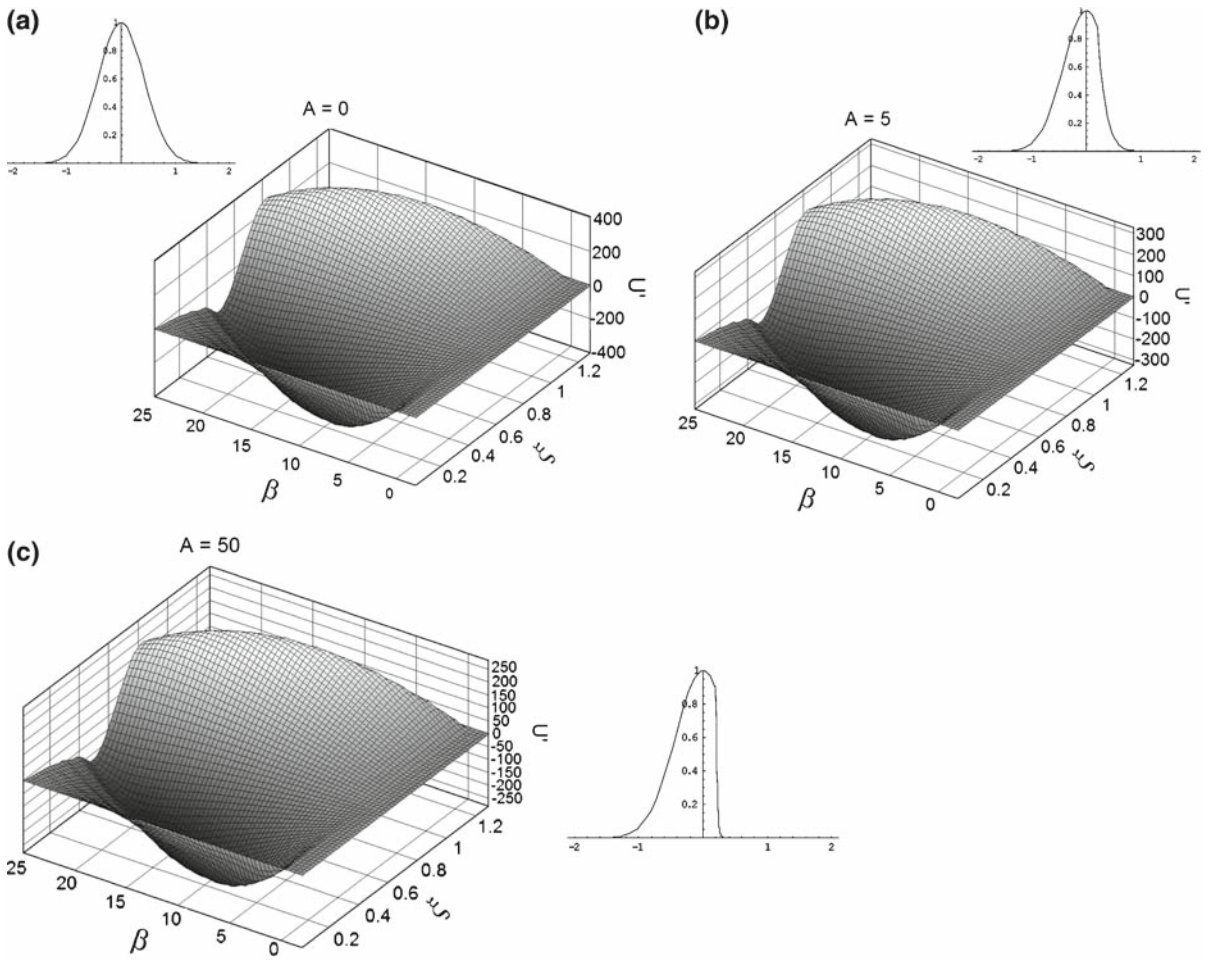

Fig. 8 Effect of plasma absorption: (**a**) $A = 0$ (no absorption), (**b**) $A = 5$, and (**c**) $A = 50$ with $\beta = 0.2$. The normalized energy density function is attached in correspondence. $H = 0.124$, $K = 6.41$, $C = 8.4 \times 10^{-3}$, $\Gamma = 100$, $M = 6.4915 \times 10^{-5}$, $Y_1 = 4.46376 \times 10^{-4}$, $Y_2 = 0.27156$, $S_0 = 500$, and $L = 1.307$

6 Discussion and conclusion

Physical phenomena of the hot-electron blast induced by ultrafast, ultraintense lasers have been further explored to include the finite speed of heat propagation in phonons, energy consumption in support of the volumetric expansion/contraction of the metal lattices, thermomechanical coupling, and thermal relaxation of phonons. The ultrafast heating and deformation are characterized by seven nondimensional groups: thermal diffusivity of electrons (K), electron-phonon coupling factor (H), laser intensity (S), heat-capacity ratio (C), relaxation time of phonons (Γ), thermomechanical coupling factor (M), elastic modulus (Y_1), and thermoelastic modulus (Y_2). Ultrafast heating of phonons is sensitive to the parameters H, M, Y, and L (film thickness), whereas ultrafast deformation is sensitive to M, Γ, Y_1 and Y_2. Three-dimensional surfaces have been prepared to examine their effects simultaneously in both space and time domains. Nonequilibrium heating emphasizes different temperatures of phonons and electrons before they come to thermal equilibrium. Inertia effects during lattice motion and volumetric expansion rate effects, which have often been neglected in classical thermoelasticity, have been found to be important in ultrafast deformation. A phenomenological approach has been adopted to assess the effect of surface to be ionization induced by high-intensity lasers. This approach modifies the energy-absorption rate through the

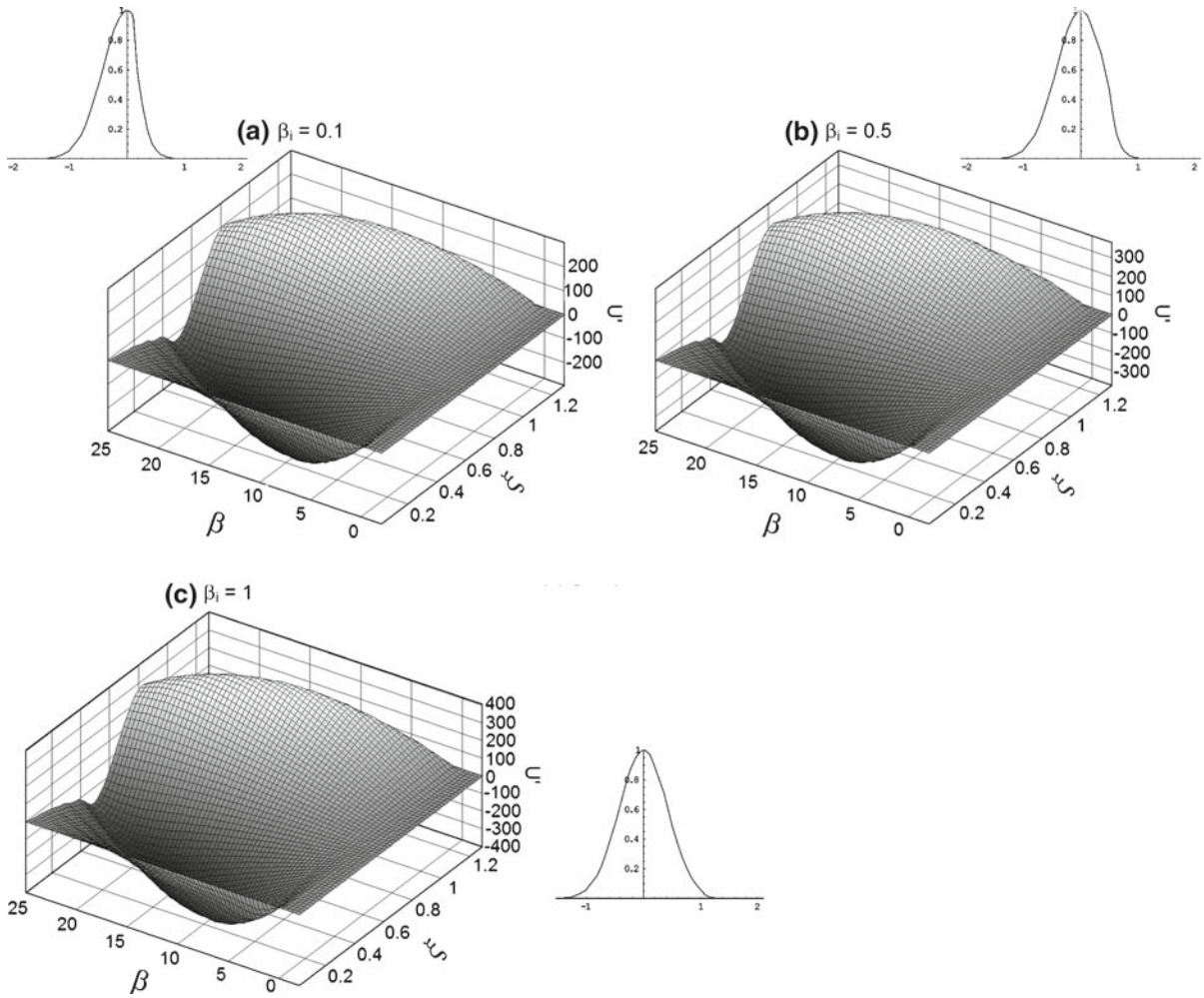

Fig. 9 Effect of plasma-formation time: (**a**) $\beta_i = 0.1$, (**b**) $\beta_i = 0.5$, and (**c**) $\beta_i = 1$ with $A = 5$. $H = 0.124$, $K = 6.41$, $C = 8.4 \times 10^{-3}$, $\Gamma = 100$, $M = 6.4915 \times 10^{-5}$, $Y_1 = 4.46376 \times 10^{-4}$, $Y_2 = 0.27156$, $S_0 = 500$, and $L = 1.307$

plasma absorption coefficient and the plasma-formation time, which can only be viewed as approximate, due to the absence of a detailed analysis of the ionic flows above the metal target.

Thermal stresses have always been difficult and complicated due to the coupling of thermal and mechanical fields and the employment of semi-empirical methods, both of which can hardly be extended universally. The finite-difference differential method employed in this work continues our efforts in microscale heat transfer by reducing the coupled PDEs to ODEs in time, which can be handled by most of the ODE solvers currently available. For easy access, we employed *Mathematica* in this work after previous implementations in IMSL and Matlab. In tackling problems with complicated structures in time, this approach has been found effective and especially suitable for beginners, facilitating a better focus on understanding the ultrafast response rather than being distracted by the various numerical algorithms for solving the nonlinearly coupled partial differential equations. Special caution, however, remains to be exercised, because the built-in subroutines in existing numerical packages, including those mentioned above, may yield questionable solutions as some parameters enter the unstable regime. With the numerical solutions thoroughly examined by different subroutines used in different packages, a detailed understanding of the method employed in those subroutines, the method of lines in *Mathematica*, for example, is critical and irreplaceable.

References

1. Lawrence Livermore National Laboratory, A New Precision Cutting Tool: The Femtosecond Laser, http://www.llnl.gov/str/Stuart.html. Credit must be given to the University of California, Lawrence Livermore National Laboratory, and the Department of Energy under whose auspices the work was performed, when this information or a reproduction of it is used.
2. Hopkins JM, Sibbett W (2000) Ultrashort-pulse lasers: Big payoffs in a flash. Sci Am 283:72–79
3. Stuart BC, Feit MD, Herman S, Rubenchik AM, Shore BW, Perry MD (1996) Optical ablation by high-power short-pulse lasers. J Opt Soc Am (B) 13:459–468
4. Shirk MD, Molian PA (1998) A review of ultrashort pulsed laser ablation of materials. J Laser Appl 10:18–28
5. Momma C, Nolte S, Chichkov BN, Alvensleben FA, Tunnermann A (1997) Precise laser ablation with ultrashort pulses. Appl Surf Sci 109:15–19
6. Preuss S, Demchuk A, Stuke M (1995) Sub-picosecond UV laser ablation of metals. Appl Phys (A) 61:33–37
7. Tzou DY, Chen JK, Beraun JE (2005) Recent development of ultrafast thermoelasticity. J Thermal Stresses 28:563–594
8. Tzou DY, Beraun JE, Chen JK (2002) Ultrafast deformation in femtosecond laser heating. ASME J Heat Transfer: Special Issue in Micro/Nanoscale Heat Transfer 124:284–292
9. Tzou DY (1997) Macro- to microscale heat transfer: the lagging behavior. Taylor & Francis, Philadelphia
10. Chen JK, Tzou DY, Beraun JE (2006) A semi-classical two-temperature model for ultrafast laser heating. Int J Heat Mass Transfer 49:307–316
11. Chen JK, Tzou DY, Beraun JE (2005) Numerical investigation of ultrashort laser damage in semiconductors. Int J Heat Mass Transfer 48:501–509
12. Rethfield B, Sokolowski-Tinten K, Linde D von der (2002) Ultrafast thermal melting of laser-excited solids by homogeneous nucleation. Phys Rev (B) 65:092103:1–092103:4
13. Xu X, Song KH (2000) Phase change phenomena during high power laser-materials interaction. Mater Sci Eng (A) 292:162–168
14. Dyer PE, Maswadi SM, Walton CD (2003) VUV F2 laser ablation of sodium chloride. Appl Phys (A) 76:817–822
15. Qiu TQ, Tien CL (1993) Heat transfer mechanisms during short-pulse laser heating of metals. ASME J Heat Transfer 115:835–841
16. Qiu TQ, Tien CL (1992) Short-pulse laser heating on metals. Int J Heat Mass Transfer 35:719–726
17. Kaganov MI, Lifshitz IM, Tanatarov MV (1957) Relaxation between electrons and crystalline lattices. Sov Phys JETP 4:173–178
18. Anisimov SI, Kapeliovich BL, Perel'man GL (1974) electron emission from metal surfaces exposed to ultra-short laser pulses. Sov Phys JETP 39:375–377
19. Anisimov SI, Rethfield B (1997) On the theory of ultrafast laser pulse interaction with metals. SPIE 3093:192–203
20. Falkovsky LA, Mishchenko EG (1999) Electron-lattice kinetics of metals heated by ultrashort laser pulses. J Exp Theoret Phys 88:84–88
21. Tzou DY (1995) A unified field approach for heat conduction from micro- to macro-scale. ASME J Heat Transfer 117:8–16
22. Tzou DY (1995) Experimental evidences for the lagging behavior in heat propagation. AIAA J Thermophys Heat Transfer 9:686–693
23. Tzou DY (1995) The generalized lagging response in small-scale and high-rate heating. Int J Heat Mass Transfer 38:3231–3240
24. Boley BA, Weiner JH (1960) Theory of thermal stresses. Wiley, New York
25. Fan CH, Sun J, Longtin JP (2002) Plasma absorption of femtosecond laser pulses in dielectrics. ASME J heat transfer 124:275–283
26. Tzou DY (2006) Computational techniques for microscale heat transfer. In: Minkowycz WJ, Sparrow EM, Murthy JY (eds) Handbook of numerical heat transfer, 2nd ed. Wiley, New York
27. Wolfram S (1999) The mathematica book. Wolfram Media/Cambridge University Press, New York